KLOE Note n. 157
March 1996

The KLOE drift chamber geometry

G. Finocchiaro,[a] F. Grancagnolo,[b] S. Spagnolo[b]

[a] Laboratori Nazionali di Frascati dell'INFN, Frascati

[b] Dipartimento di Fisica dell'Università e Sezione INFN, Lecce

ABSTRACT

The considerations which led to the final design of the cell structure of the KLOE drift chamber are reviewed. Maps of the hole positions in the chamber end plates are given, along with distributions of several quantities entering in the definition of the cell geometry.

1. Introduction: basic criteria

The physics requirements for the KLOE drift chamber are discussed detailedly in [1]: here we will mention few points. Everything is of course devoted to the final aim of the detection of K decays with high and well controlled efficiency, and with spatial resolution $\sigma_{R\phi} \leqslant 200\,\mu$m. We take for granted the choice of having square cells with only stereo wires, which guarantees the most uniform and efficient filling of the tracking volume.

The high granularity of the tracking chamber, required in order to finely sample the tracks, must balance the need of controlling the total number of wires in order to reduce the mechanical tension on the end plate walls, eventual wire breaking casualities, the number of electronic channels and the scattering on the wires. Also, construction time considerations are relevant, since reducing the total number of wires makes not only faster but also technically easier the stringing phase. A cell size of $3\times 3\,\mathrm{cm}^2$, according to detailed Monte Carlo studies, guarantees the desired efficiency and resolutions and involves a total number of wires of the order of $5{\cdot}10^4$, which is still acceptable from the technical point of view.

Another relevant point is the "uniformity" of the cells over the tracking volume. As we shall see in the following, arranging square cells in a cylindrical volume forces one to have differences among the shapes of the cell themselves. These differences we tried to minimise, in the belief that this will be a benefit during the analysis of the chamber data.

Following this philosophy, the ratio of field to sense wires, $\mathcal{R}_{\mathrm{fs}}$, has been chosen to be 3:1, to ensure a safety margin on the uniformity of the space-time relations with the azimuthal angle. Other considerations which have contributed to this choice are the minimization of the mechanical tension on the end walls and of the wire contribution to the multiple scattering of the particles in the chamber. A larger $\mathcal{R}_{\mathrm{fs}}$ in fact, allows the use of thinner field wires for the same value of the electric field on the surface of the wires, which sets the gain of the chamber.

2. The frame of the KLOE drift chamber

There are two key requirements, to some extent in mutual conflict, to be met in the design of the frame of the KLOE drift chamber, namely the detection of a substantial fraction of K_{L} decays, and the transparency for particles, especially photons, which eventually reach the calorimeter. The solution is a chamber of huge dimensions, of essentially cylindrical symmetry, with the frame entirely in carbon fiber. It schematically consists of two End-Plates (EP) kept apart by twelve rods. Gas tightness is provided by a thin cylinder on the inner side, and by twelve panels glued on the rods at the outer radius.

The EP are spherical because this shape minimises, for fixed plate thickness, the longitudinal deformation due to the wire tension. The plate design is shown in fig. 1, while the general structure of the chamber is shown in fig. 2.

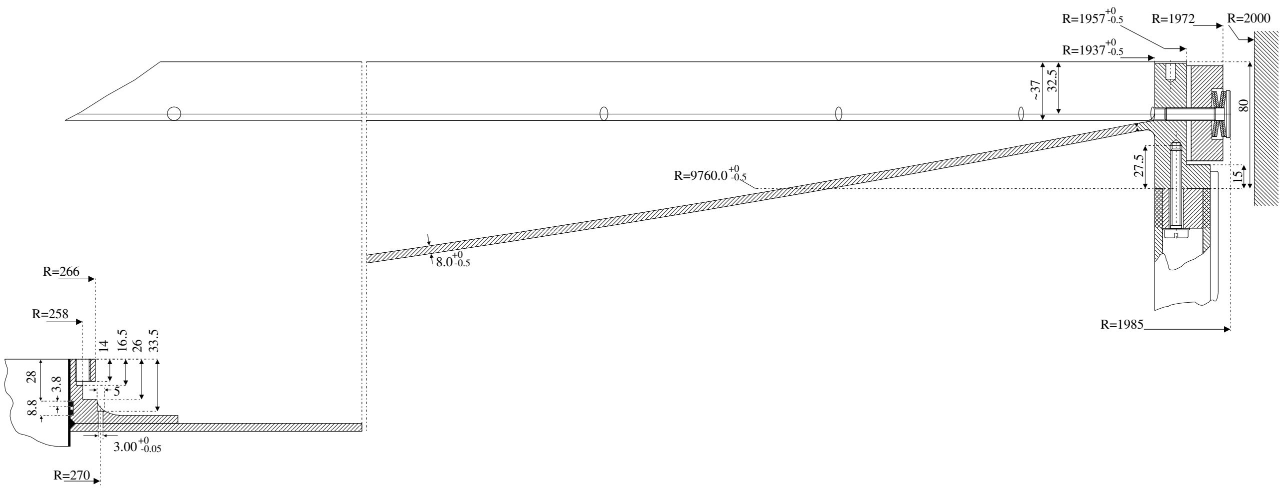

Fig. 1: *Technical drawing of the end plate of the KLOE drift chamber.*

We have inferred the dimensions of the chamber from the technical drawings reproduced in the figures above. The main parameters are listed in tab. 1.

Quantity	Value
Max. plate radius (R_{out})	1937.00 mm
Plate curv. radius	9768.00 mm
Plate dist. @ R_{out}	3229.68 mm
Plate thickness	8.00 mm

Tab. 1: *Main parameters of the KLOE drift chamber geometry.*

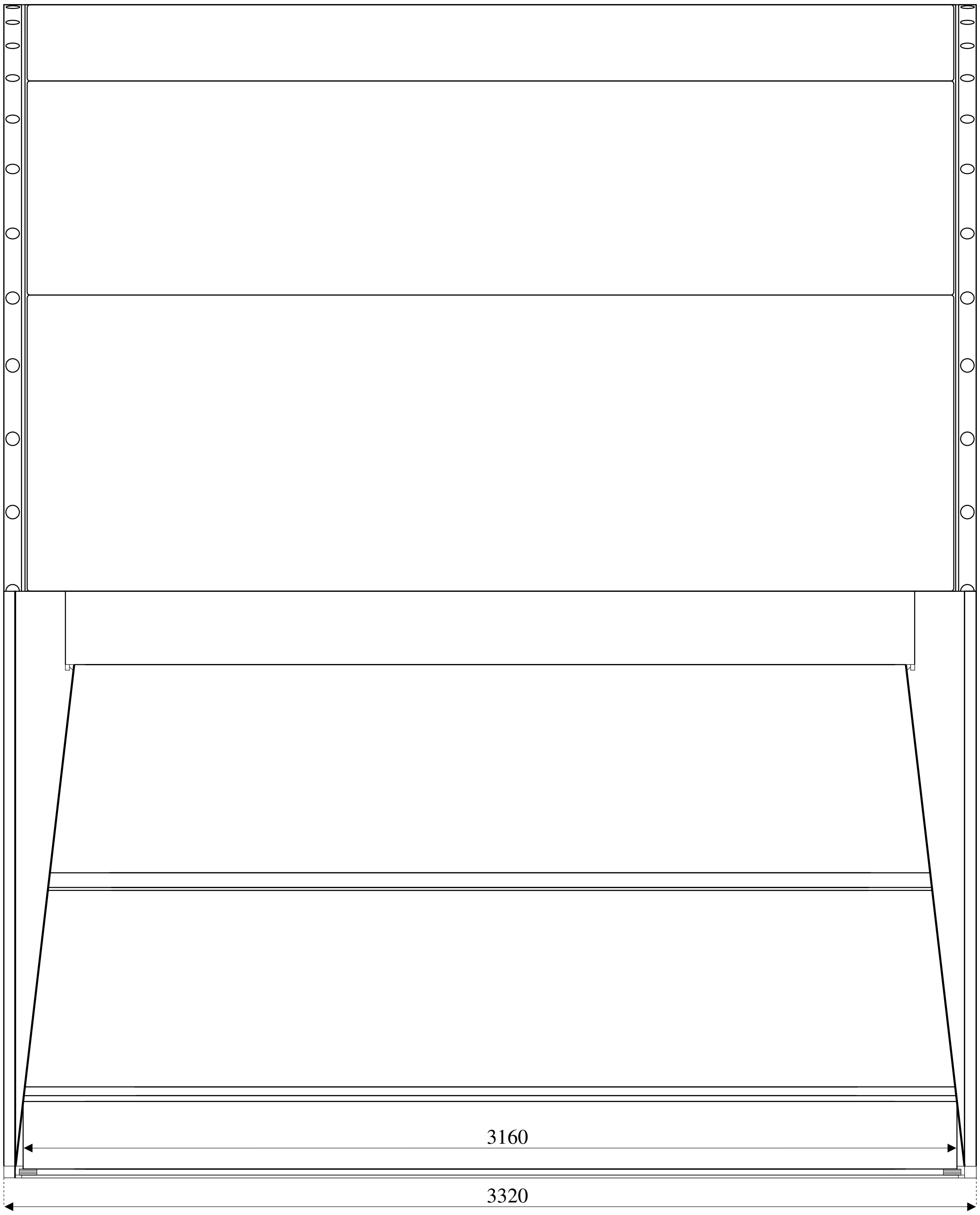

Fig. 2: *Side view of the KLOE drift chamber structure.*

In the calculations reported in the following chapters we have taken into account all the details at our knowledge. An example of this is seen in fig. 3, where the particular of the insertion of a feed-through into the EP wall is shown.

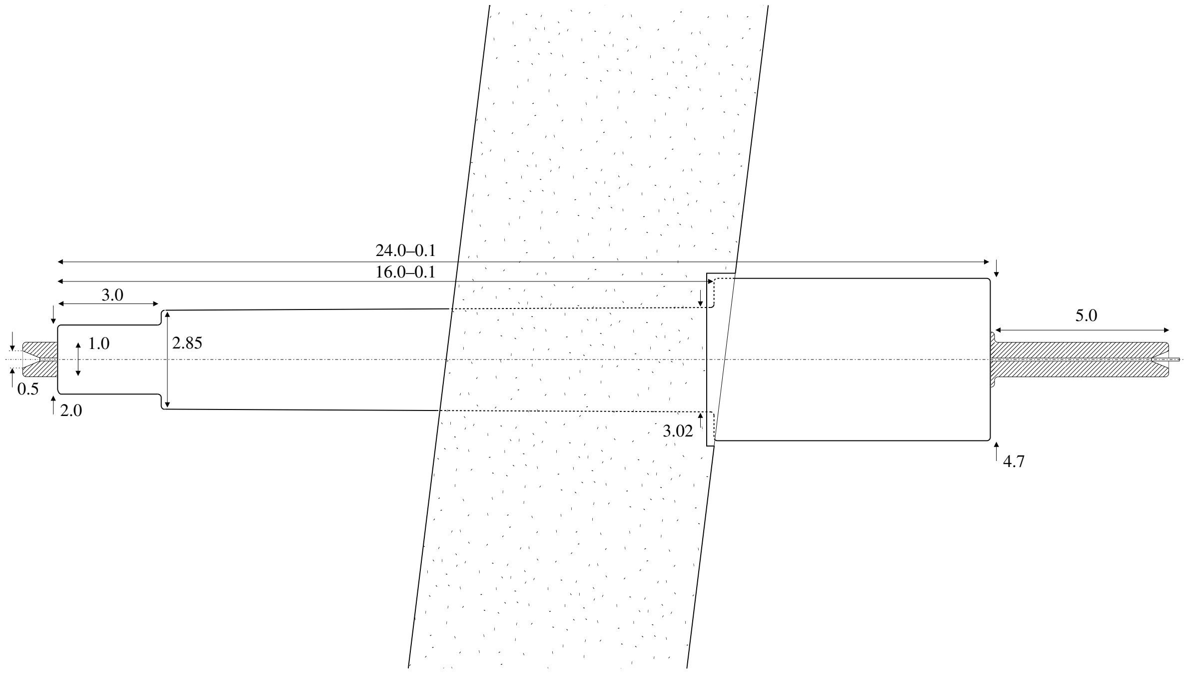

Fig. 3: *Detail of the insertion of a feed-through into the EP wall.*

3. Conventions and basic definitions

We will give some definitions and basic relations among useful geometrical quantities related to the structure of the KLOE drift chamber. In the following we assume the global reference frame already defined for the detector and we try to be consistent with all the previously stated conventions [2].

As we already mentioned, the chamber volume is sampled by single wire active cells arranged in adjacent circular coaxial layers. The requirement to achieve a tridimensional reconstruction of charged tracks in the detector, without loss of uniformity in the cell response and in the full coverage of the gas volume, naturally leads to arrange all the cells of the same layer at an angle (the *stereo angle* ε_j) with respect to the chamber axis, the sign of which changes from one layer to the following. We call P_A and P_B respectively the points of the end plates A and B to which a wire is connected (see appendix A for the reference system). The stereo angle ε_j is the angle between the wire and an ideal axial wire starting from P_A and running parallel to the z axis. As a consequence of the stereo angle, the distance of the wire from the chamber axis varies continuously along z, reaching its maximum value $R_{\text{E.P.}}$ at the end plates, and being minimum at $z = 0$ ($R_{z=0}$). The difference $\delta \equiv R_{\text{E.P.}} - R_{z=0}$ is called the *stereo drop*. The azimuthal angle of the wire, φ, also depends on z because of the stereo geometry.

A relevant parameter is $\alpha \equiv (\varphi^{\text{B}}_{\text{E.P.}} - \varphi^{\text{A}}_{\text{E.P.}})$: it depends just on the ratio between δ and the radius:

$$\alpha = 2 \cdot \text{atan}\left(\frac{\delta}{R_{z=0}} \sqrt{2\frac{R_{z=0}}{\delta} + 1} \right).$$

The sign of the stereo angle is set equal to the sign of α.

In this sign convention, the distance of the intersection of a wire with a plane perpendicular to the chamber axis as a function of z is given by:

$$R(z) = \sqrt{R^2_{z=0} + (z \cdot \tan\varepsilon)^2}, \tag{1}$$

while the corresponding azimuthal coordinate is:

$$\varphi(z) = \varphi_{z=0} + \text{atan}\left(\frac{z \cdot \tan\varepsilon}{R_{z=0}} \right).$$

From fig. 4 the relation between the drop, the distance between the end plates and the stereo angle is worked out to be:

$$\varepsilon_j = \text{atan}\left(\frac{2\delta}{L(R^j_{\text{E.P.}})} \sqrt{\frac{2R^j_{\text{E.P.}}}{\delta} - 1} \right),$$

j being the wire layer index. Since the EP are spherical, the distance between them is a (mildly varying) function of the radius: $L = L(R^j_{\text{E.P.}})$.

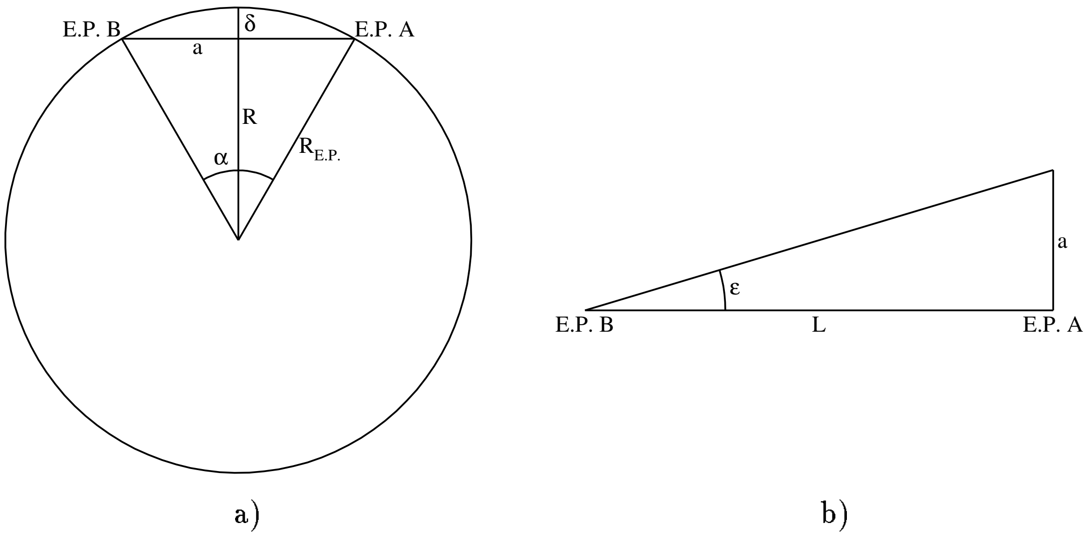

Fig. 4: *Illustration of the parameters in the text. a): the chamber as seen from one End-Plate; b) top view.*

We choose to keep δ constant to minimise the radial cell deformation along the longitudinal direction. Again Monte Carlo studies have shown that δ=1.5 cm is an adequate compromise between the z resolution ($\sigma_z \sim \sigma_{R\phi}/\tan\varepsilon_j$) and the fact that the stereo angle can not be made big at will.

In the all stereo structure of the detector, only square cells can keep the original shape from one end plate to the other and provide, at the same time, a reasonably isotropic response.

A ratio between field and sense wires $\mathcal{R}_{\rm fs}$ equal to 3:1 appears to be a satisfactory solution to ensure good electrostatic definition of the cell without affecting the detector transparency. Since a layer shares with the neighbouring ones the field wires closing upward and downward the cell area, we define *cell layer* the set of a field *wire layer* and the field+sense *wire layer* above it. Therefore, the field wires which constitute the upper boundary of the layer belong by definition to the following layer and are strung at a stereo angle of opposite sign with respect to the sense wire layer immediately below them. This feature results in an electrostatic field at the upper edge of the cell periodically varying with z.

In order to fit an integer number of cells N_s^i in a layer, the size of the cell must be suitably chosen. We define the *nominal cell width* w as the length of the arc between the left and the right edge of the cell in the plane $z = 0$ (in the following, unless explicitly stated, the radii refer to this plane, and i is the cell layer index) at radius R^i. Thus, the number of cells in the $i-th$ layer is

$$N_s^i = \frac{2\pi R^i}{w}.$$

Since front-end electronic cards have a channel multiplicity of 6, we have chosen N_s^i to be multiple of 6 as well:

$$\Delta N = N_s^{i+1} - N_s^i = \frac{2\pi h}{w} = 6k,$$

where h is the cell height and k is an integer.

4. Possible solutions

The contraints discussed above lead to the following, quite natural, choice:

$$h = 3\,\mathrm{cm}, \quad \Delta N = 6 \text{ (or } k = 1) \implies w = \pi\,\mathrm{cm},$$

with R^1 extracted from the sequence $24, 27, 30, 33, ...$ cm. Specialising now the definition of w and R^i as width and radius at the top of the cell, we get, at the plane $z = 0$, a ratio between the width w_s of the cell at the sense wire radius R_s^i and its height h sligthly increasing with the layer radius:

$$\frac{w_s}{h} = \frac{2\pi R_s^i}{h N_s^i} = \frac{w}{h} \cdot \frac{R_s^i}{R_s^i + h/2}. \tag{2}$$

Taking into account the quadrupoles sizes, the maximum available radius, the improved gain stability deriving from the use of guard wires before and after the layers of sensitive cells, and assuming a value for the stereo drop of δ=1.5 cm, the most efficient filling of the drift volume is obtained in the following way:

a) the inner guard wire layer is placed at the radius $R_{g1} = 26\,\mathrm{cm}$;

b) the lower edge of the first layer starts at $R_{\mathrm{lower}} = 27\,\mathrm{cm}$, therefore $R_{\mathrm{upper}} \equiv R^1 = 30\,\mathrm{cm}$ and the first sense wires are placed at $R_s^1 = 28.5\,\mathrm{cm}$;

c) the total number of layers is 54 and the outer edge of the sampled active volume is at $R^{54} = 189\,\mathrm{cm}$;

d) the radius of the outer guard wire layer is $R_{g2} = 190\,\mathrm{cm}$.

This configuration accounts for a total number of active cells N_s equal to 11 826 and a grand total of 48 960 wires in the chamber.

A high granularity region in the core of the tracking chamber is of some interest, since it can provide an improved reconstruction efficiency for short tracks coming from vertices close to the fiducial volume boundary and propagating backward. A mixed cell size design can be easily implemented by modifying the $3 \times \pi\,\mathrm{cm}^2$ structure described above.

A possible solution is to split some of the innermost layers into a double number of layers of almost square 1.5 cm high cells. Defining R_{break} as the radius of the boundary region, the layers with $R \geq R_{\mathrm{break}}$ are unchanged. The modularity of 6 in the electronic cards imposes to fit the same number of cells into two consecutive small cell layers. For this reason the aspect ratio (w_s/h), while increasing separately for even and odd layers, goes up and down from one layer to the next one.

$N_{\text{Layer}}^{\text{Tot}}$	$N_{\text{Layer}}^{\text{small}}$	$w \times h$ (cm^2)	R_0^1 (cm)	R_{break} (cm)	N$_{s.w.}$	N$_{f.w.}$	N$_{g.w.}$
54	0	$\pi\times3$	28.50	✓	11826	36246	888
58	8	$\pi\times3$ and $\pi/2\ \times1.5$	27.75	39.0	12 654	38 898	1008
60	12	$\pi\times3$ and $\pi/2\times1.5$	27.75	45.0	13 176	40 488	1008
57	9	$\pi\times3$ and $2\pi/3\times2$	28.00	45.0	12 348	37 908	936
58	12	$\pi\times3$ and $2\pi/3\times2$	28.00	51.0	12 582	38 622	936
59	15	$\pi\times3$ and $2\pi/3\times2$	28.00	57.0	12 846	38 658	936
60	18	$\pi\times3$ and $2\pi/3\times2$	28.00	63.0	13 140	40 320	936

Tab. 2: *Main features of a possible uniform design of the KLOE drift chamber geometry and of some mixed cell size designs*

A different solution is to substitute an even number N_{big} of $3\times\pi$ cm^2 cell layers with $N_{\text{small}} = 3/2 \times N_{\text{big}}$ layers of 2 cm high cells. The remaining layers are unchanged if N_{small} is even, otherwise the stereo angles of layers with $R \geq R_{\text{break}}$ get a -1 sign.

It is convenient to define the nominal width and radius of the small cell layers as quantities at the sense wire ($w = w_s = 2\pi/3$ cm and $R^i = R^i_s = 28, 30, 32, ...$ cm). In this case the number of cells in a layer is given by $N^i_s = 3R^i_s$ and the aspect ratio is constant (at $z = 0$).

In these mixed configurations, in order to guarantee that the outermost layer of small cells have a well defined electrostatic boundary, the number of wires in the upper field wire layer ($R = R_{\text{break}}$) is increased. As seen from the first “big cell” layer above, this corresponds to say that below each sense wire of such a layer there are 3 (for $2\pi/3\times2$ cm^2 small cells) or 4 (for $\pi/2\times1.5$ cm^2 small cells) field wires.

The main features of the described configurations are listed in tab. 2 above.

5. The chamber design

Among the solutions pointed out in the previous chapter, we have chosen the mixed structure with $N_{\text{small}} = 12$ layers of $2\pi/3\ \times2$ cm^2 size cells. As we have repeatedly stressed, the upper cell shape is different for every cell in a layer (unless accidental periodicity) and for a single cell it changes with z. Therefore, the start angle for each cell layer is a pure matter of convention. We arbitrarely imposed that, in the plane $z = 0$, each cell layer has a sense wire at φ=0; in the field wire layer below, a field wire is radially aligned to the upper sense wires, with the only exception of the 13-*th* layer, whose lower edge consists of a number of wires $N_f = 3 \times N^{13}_s$.

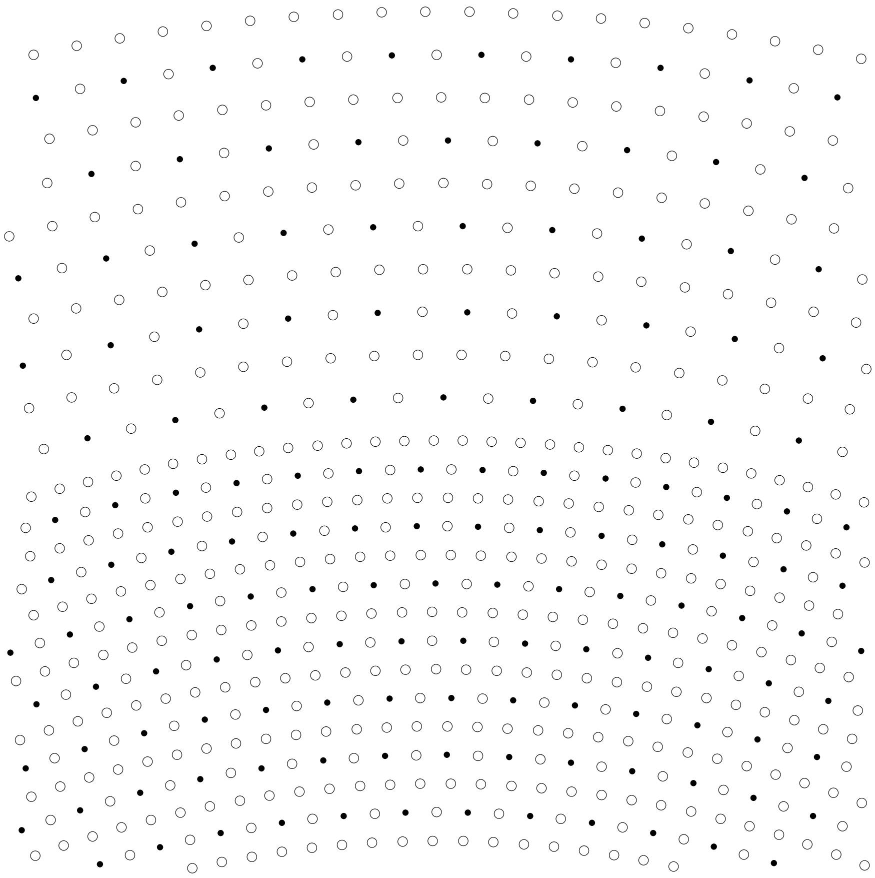

Fig. 5: *Detail of the hole map in the boundary region between small and big cells. The circles represent field wires, the dots sense wires.*

The choice of locating the intersection of the wire with the $z = 0$ plane symmetrically with respect to the x axis allows to have hole maps which turn out to be equal on both end plates. In other words, EP A can be exactly superimposed to EP B, hole map included, provided a $180°$ rotation around its x axis is performed (see appendix A for details on the conventions adopted).

A detail of the hole map centered at (0.0,52.5), therefore including the transition region between $\pi \times 3\,\mathrm{cm}^2$ and $2\pi/3 \times 2\,\mathrm{cm}^2$ cells, is presented in fig. 5.

The number of cells in a layer and the starting φ at $z = 0$, given the maximum stereo drop δ, uniquely define α, the angle of displacement of the wires from EP B to EP A (see fig. 4). α in turn determines the location of the feed-through holes on the end plates. The hole map is given in appendix A along with other relevant quantities, among which the stereo angle, as calculated from the chamber geometry of § 2. Such figure is realistic, but not really final, in the sense that the drift chamber dimensions will be definitive only after the assembly.

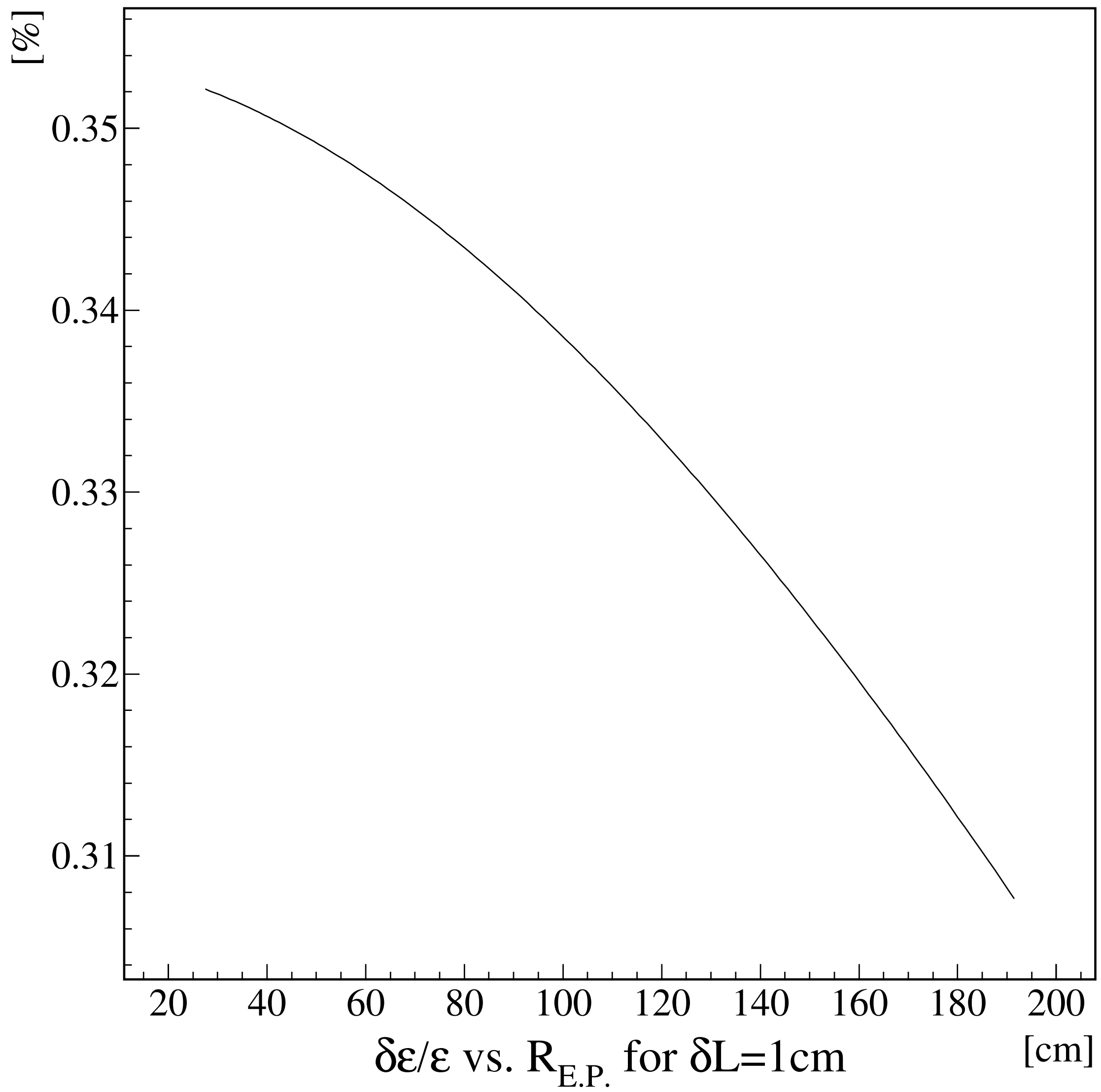

Fig. 6: *Relative variation of the stereo angle for a change of $\delta L = 1\,\mathrm{cm}$ of the plate distance wrt. the nominal dimension.*

However, we expect that the deviations from the nominal chamber length will be of the order of a few mm. In fig. 6 it is shown that, for $\delta L = 1\,\mathrm{cm}$, the relative variations of the stereo angles are $< 0.4\%$, *i.e.* so small that the correction with the surveyed chamber dimensions, although certainly feasible, will probably be irrelevant.

The cell size is constant troughout the volume of the detector except for small effects, connected with the stereo geometry:

a) the cell height slightly decreases with $|z|$ from the plane $z = 0$ towards the end plates (fig. 7a);

b) the cell width increases with $|z|$, eqn. (1) – an effect ~ 20 times more important than the previous one, see fig. 7b;

c) as a consequence, also the aspect ratio w/h increases with z (fig. 7c). As it is evident from eqn. (2) and from the differences among the three representative layers shown in fig. 7, the aspect ratio depends also on the radius (fig. 7d).

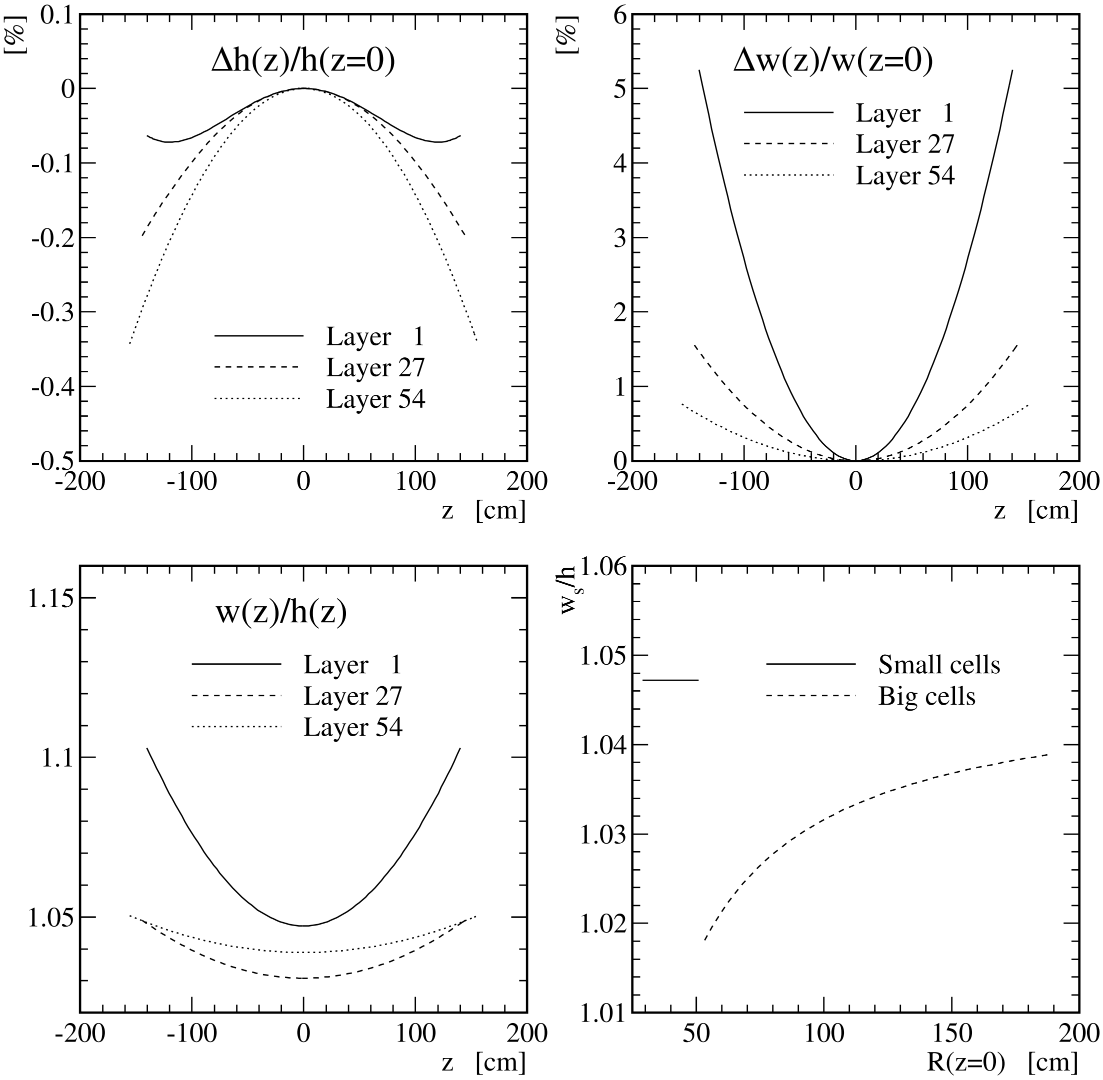

Fig. 7: *Relative variation of the cell height (a), width (b) and aspect ratio (c) along the longitudinal axis of the chamber for some layers. (d) is a graphic representation of eqn. (2).*

The cell shape, that is the position of the field wires with respect to the central sense wire, is a further relevant point. As it is seen from fig. 5, the position of the upper field layer of each cell with respect to the field+sense layer below it, changes with the radius. Moreover, since these layers are not parallel, their relative position changes along z, and after a certain period $T_D(z)$ the set of upper field wires closest to the sense wire will change.

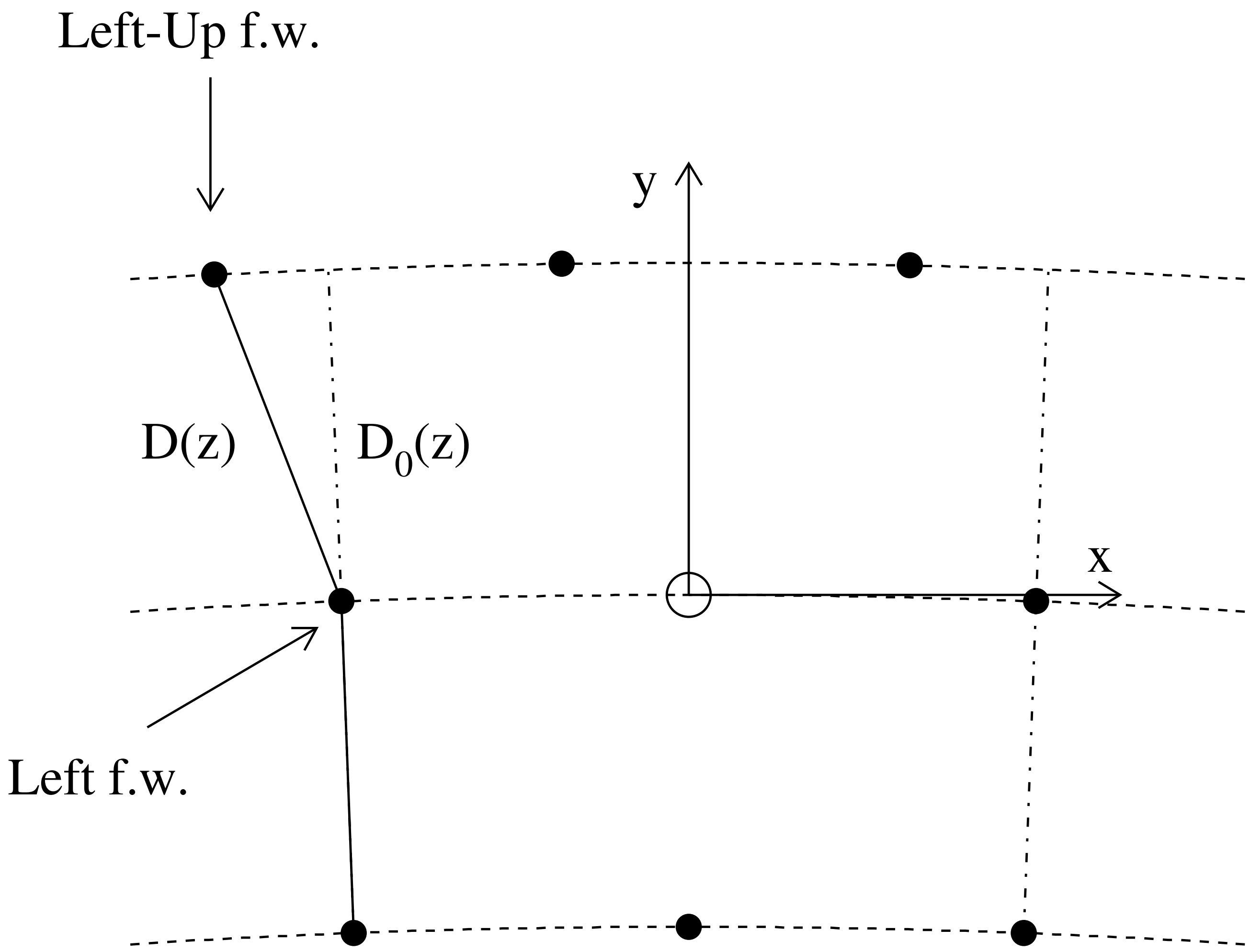

Fig. 8: *A pictorial representation of a typical cell of the KLOE drift chamber.*

The resulting cell shape deformation can be described by the relative variation of the distance D between the upper-left field wire and the left field wire (see fig. 8) with respect to the reference case in which the two wires are radially aligned. Fig. 9 shows this effect as a function of z for three different layers. The sudden jumps in $\Delta D/D$ correspond to changes of the upper field wire set. As a consequence of the slight variation of the cell width, the z separation between these discontinuities (period) is not exactly constant, as shown in fig. 10.

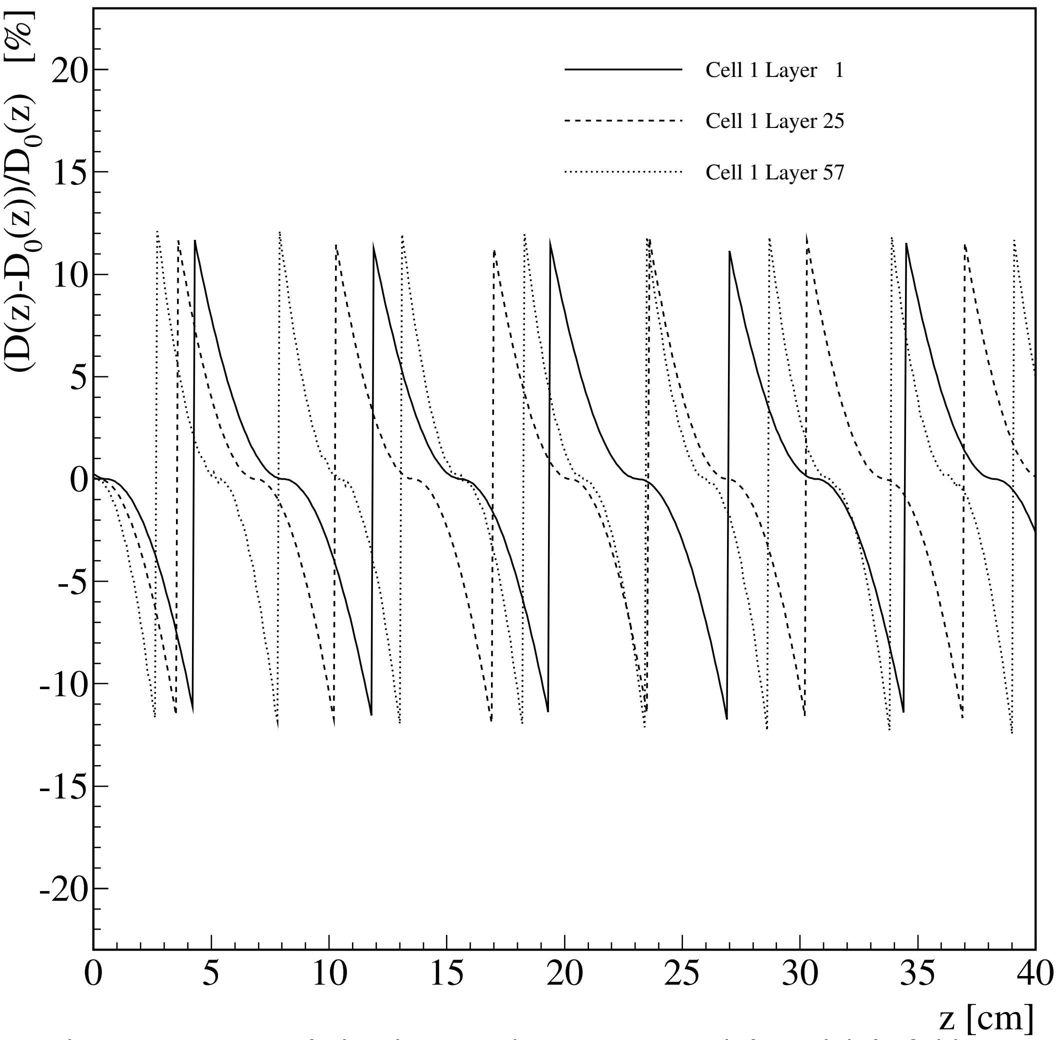

Fig. 9: *Relative variation of the distance between upper-left and left field wires. Plus (minus) signs are assigned to cases with upper field wires at the right (left) of the configurazion with the two wires radially aligned (for which $D(z) = D_0(z)$).*

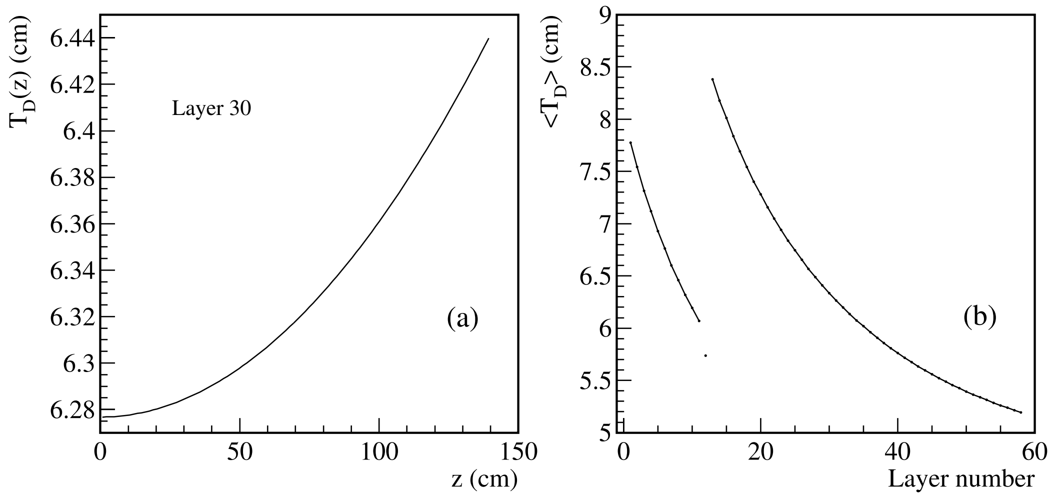

Fig. 10: *(a): z separation between consecutive changes in the set of upper field wires vs. z; (b): average periodicity in the upper edge of the cell vs. layer #. Notice the leap in $T_D(z)$ at the end of 2×2 region and its special value at the 12-th layer.*

APPENDIX A: Hole maps & reference system

This appendix essentially consists of a table which summarizes the most relevant cell geometry figures. The columns list, respectively:

1. layer number;
2. type of cell layer: G/F/S stand respectively for Guard, Field, and Sense layer. Sense layers consist of alternating sense and field wires;
3. layer radius at the end plates;
4. stereo angle;
5. angle of the first hole on the EP;
6. number of wires on the layer. For the 'S' type, half of these wires are sense, half are field;
7. number of holes to skip in order to string the wires with the correct stereo angle.

Some more details are in order to make point 5 above unambiguous. In the DC global reference system (which is the same as the KLOE one) the x axis is horizontal, oriented as the radius connecting the DAΦNE ring and the KLOE centers; the y axis is vertical, positive upwards; the z axis is along the bisetrix of the e^+e^- crossing angle, positive along the positron motion. End plate A is placed at $z < 0$, EP B at $z > 0$.

Dealing now with the hole positions, we consider the end plates from their concave side, *i.e.* from outside the chamber; this in a sense is a natural choice, since the holes will be drilled from this side.

The reference frame of EP B coincides with the global one ($x_{\rm B} = x_{\rm global}$, $y_{\rm B} = y_{\rm global}$): angles are counted counterclockwise, starting from the x axis. One easily realises that hole positions on EP A have the same coordinates as on EP B, provided the $x_{\rm A}$ axis is the projection on end plate A of the global x axis, and $y_{\rm A} = -y_{\rm global}$, with the angles still counted counterclockwise.

I	Type	$R_{\mathrm{E.P.}}$	ε	φ_0	$\mathrm{N}_{\mathrm{wires}}$	$\Delta\mathrm{N}$
1	G	27.5	+63.177	32.610	168	+16
2	F	28.5	−64.331	10.716	168	−18
3	S	29.5	−65.463	16.336	168	−18
4	F	30.5	+66.575	0.766	180	+18
5	S	31.5	+67.666	30.592	180	+16
6	F	32.5	−68.738	22.247	192	−20
7	S	33.5	−69.792	26.868	192	−20
8	F	34.5	+70.829	18.764	204	+18
9	S	35.5	+71.849	14.535	204	+18
10	F	36.5	−72.853	3.206	216	−20
11	S	37.5	−73.842	7.094	216	−20
12	F	38.5	+74.816	4.481	228	+20
13	S	39.5	+75.776	0.890	228	+20
14	F	40.5	−76.721	14.967	240	−22
15	S	41.5	−77.654	18.296	240	−22
16	F	42.5	+78.573	17.139	252	+20
17	S	43.5	+79.480	14.041	252	+20
18	F	44.5	−80.376	1.419	264	−22
19	S	45.5	−81.259	4.312	264	−22
20	F	46.5	+82.131	4.271	276	+22
21	S	47.5	+82.992	1.562	276	+22
22	F	48.5	−83.842	12.446	288	−24
23	S	49.5	−84.681	14.990	288	−24
24	F	50.5	+85.511	13.957	300	+22
25	S	51.5	+86.330	11.562	300	+22
26	F	52.5	−87.140	2.788	324	−25
27	S	54.0	−88.337	25.548	216	−18
28	F	55.5	+89.514	12.559	228	+16
29	S	57.0	+90.671	9.459	228	+16
30	F	58.5	−91.808	8.677	240	−18

I	Type	$R_{\mathrm{E.P.}}$	ε	φ_0	$\mathrm{N}_{\mathrm{wires}}$	$\Delta\mathrm{N}$
31	S	60.0	−92.928	11.544	240	−18
32	F	61.5	+94.029	21.848	252	+16
33	S	63.0	+95.113	19.187	252	+16
34	F	64.5	−96.180	21.914	264	−20
35	S	66.0	−97.230	0.593	264	−18
36	F	67.5	+98.264	6.324	276	+18
37	S	69.0	+99.283	4.008	276	+18
38	F	70.5	−100.287	11.514	288	−20
39	S	72.0	−101.276	13.686	288	−20
40	F	73.5	+102.250	13.880	300	+18
41	S	75.0	+103.210	11.839	300	+18
42	F	76.5	−104.156	3.030	312	−20
43	S	78.0	−105.089	4.952	312	−20
44	F	79.5	+106.009	0.638	324	+20
45	S	81.0	+106.915	18.215	324	+18
46	F	82.5	−107.809	14.717	336	−22
47	S	84.0	−108.691	16.435	336	−22
48	F	85.5	+109.560	7.041	348	+20
49	S	87.0	+110.417	5.412	348	+20
50	F	88.5	−111.263	7.610	360	−22
51	S	90.0	−112.097	9.158	360	−22
52	F	91.5	+112.919	12.417	372	+20
53	S	93.0	+113.730	10.945	372	+20
54	F	94.5	−114.531	1.576	384	−22
55	S	96.0	−115.320	2.979	384	−22
56	F	97.5	+116.099	1.104	396	+22
57	S	99.0	+116.868	15.632	396	+20
58	F	100.5	−117.626	11.810	408	−24
59	S	102.0	−118.374	13.090	408	−24
60	F	103.5	+119.111	5.898	420	+22

I	Type	$R_{\text{E.P.}}$	ε	φ_0	N_{wires}	ΔN	I	Type	$R_{\text{E.P.}}$	ε	φ_0	N_{wires}	ΔN
61	S	105.0	+119.839	4.673	420	+22	91	S	150.0	−137.623	5.068	600	−28
62	F	106.5	−120.558	6.499	432	−24	92	F	151.5	+138.095	7.370	612	+26
63	S	108.0	−121.266	7.673	432	−24	93	S	153.0	+138.560	6.676	612	+26
64	F	109.5	+121.965	10.046	444	+22	94	F	154.5	−139.018	1.509	624	−28
65	S	111.0	+122.655	8.920	444	+22	95	S	156.0	−139.470	2.182	624	−28
66	F	112.5	−123.335	1.866	456	−24	96	F	157.5	+139.914	9.693	636	+26
67	S	114.0	−124.007	2.947	456	−24	97	S	159.0	+140.352	9.039	636	+26
68	F	115.5	+124.669	0.232	468	+24	98	F	160.5	−140.783	8.620	648	−30
69	S	117.0	+125.322	12.618	468	+22	99	S	162.0	−141.207	9.256	648	−30
70	F	118.5	−125.967	10.890	480	−26	100	F	163.5	+141.625	2.281	660	+28
71	S	120.0	−126.602	11.891	480	−26	101	S	165.0	+142.036	1.663	660	+28
72	F	121.5	+127.230	4.049	492	+24	102	F	166.5	−142.441	5.917	672	−30
73	S	123.0	+127.848	3.084	492	+24	103	S	168.0	−142.839	6.519	672	−30
74	F	124.5	−128.458	6.680	504	−26	104	F	169.5	+143.231	4.533	684	+28
75	S	126.0	−129.060	7.609	504	−26	105	S	171.0	+143.617	3.947	684	+28
76	F	127.5	+129.654	7.423	516	+24	106	F	172.5	−143.996	3.442	696	−30
77	S	129.0	+130.239	6.526	516	+24	107	S	174.0	−144.369	4.013	696	−30
78	F	130.5	−130.817	2.934	528	−26	108	F	175.5	+144.736	6.594	708	+28
79	S	132.0	−131.386	3.801	528	−26	109	S	177.0	+145.097	6.037	708	+28
80	F	133.5	+131.948	10.421	540	+24	110	F	178.5	−145.452	1.168	720	−30
81	S	135.0	+132.501	9.583	540	+24	111	S	180.0	−145.800	1.710	720	−30
82	F	136.5	−133.047	10.970	552	−28	112	F	181.5	+146.143	8.483	732	+28
83	S	138.0	−133.585	0.398	552	−26	113	S	183.0	+146.479	7.954	732	+28
84	F	139.5	+134.116	1.954	564	+26	114	F	184.5	−146.810	7.520	744	−32
85	S	141.0	+134.639	1.169	564	+26	115	S	186.0	−147.135	8.037	744	−32
86	F	142.5	−135.155	7.493	576	−28	116	F	187.5	+147.454	1.909	756	+30
87	S	144.0	−135.663	8.253	576	−28	117	S	189.0	+147.768	1.405	756	+30
88	F	145.5	+136.164	4.801	588	+26	118	F	190.5	−148.075	5.326	768	−32
89	S	147.0	+136.657	4.065	588	+26	119	G	191.5	−148.277	5.655	768	−32
90	F	148.5	−137.144	4.354	600	−28							

Tab. 3: *Map of the holes on EP A. The columns contain, respectively: layer number; layer type (G/F/S for Guard/Field/mixed Sense+field); radius at the EP (cm); stereo angle (mrad) ; angle of the first hole (mrad); # of wires on the layer; # of holes (with sign) to skip in order to string the wires at the correct stereo angle.*

APPENDIX B: A few distributions

We illustrate here some other features of the chosen geometrical configuration of the KLOE drift chamber. Figs. 11 and 12 show, respectively, the stereo angle and the angle, in the $x - y$ plane, between the straight lines connecting the origin of the reference frame to the holes on the end plates to which a wire will be hung, as a function of the radius of the wire layer at the end plate.

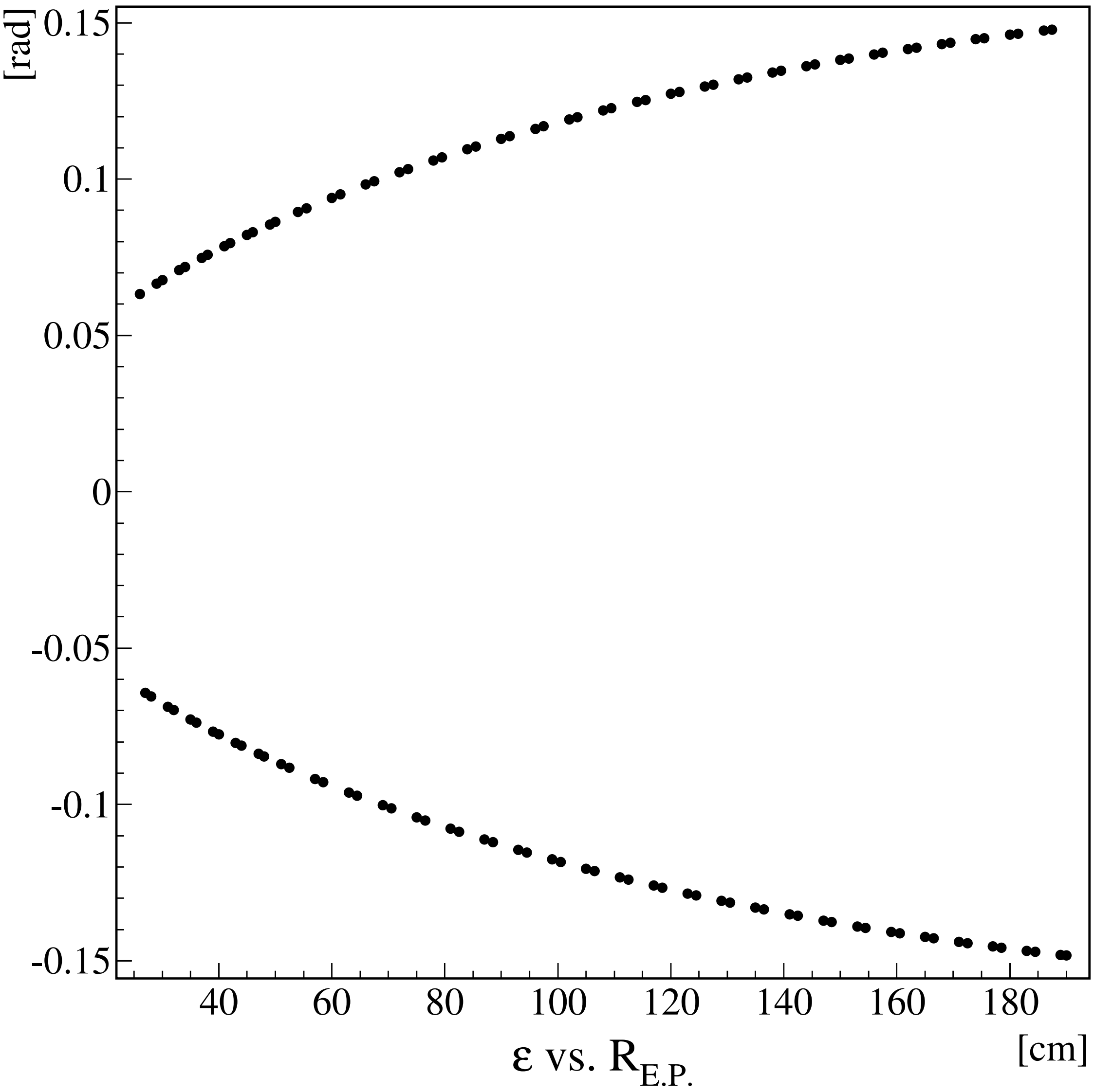

Fig. 11: *Stereo angles vs. radius on the End-Plates.*

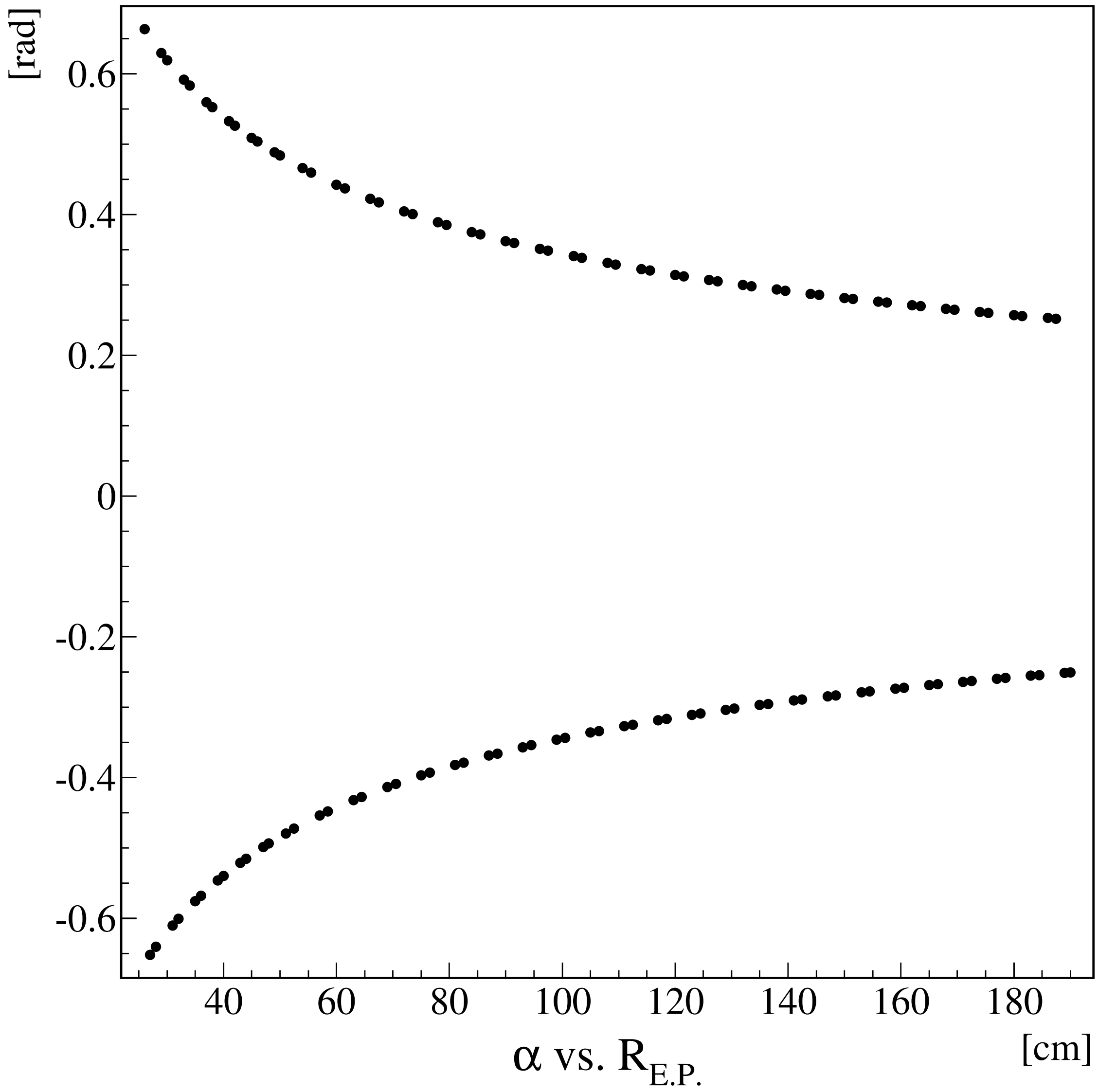

Fig. 12: *Plate-plate displacement angles vs. radius on the End-Plates.*

Finally, fig. 13 shows cell width distributions for small and big cells in the plane $z = 0$ and on the end plates. The real width of small cells at the center of the KLOE drift chamber is fixed since, by design, it corresponds to the nominal one; on the contrary, at the end plates the same quantity has a small spread (around a value slightly larger than for $z = 0$). For big cells the effective width in the plane $z = 0$ depends on the layer because the nominal cell width constrains the size of the cell at the radius of the outer boundary. Since, by construction, the value of the stereo drop is equal to the half-height of the cell, the effective cell width at the end plates is forced to match its nominal value and, therefore, does not depend on the layer radius.

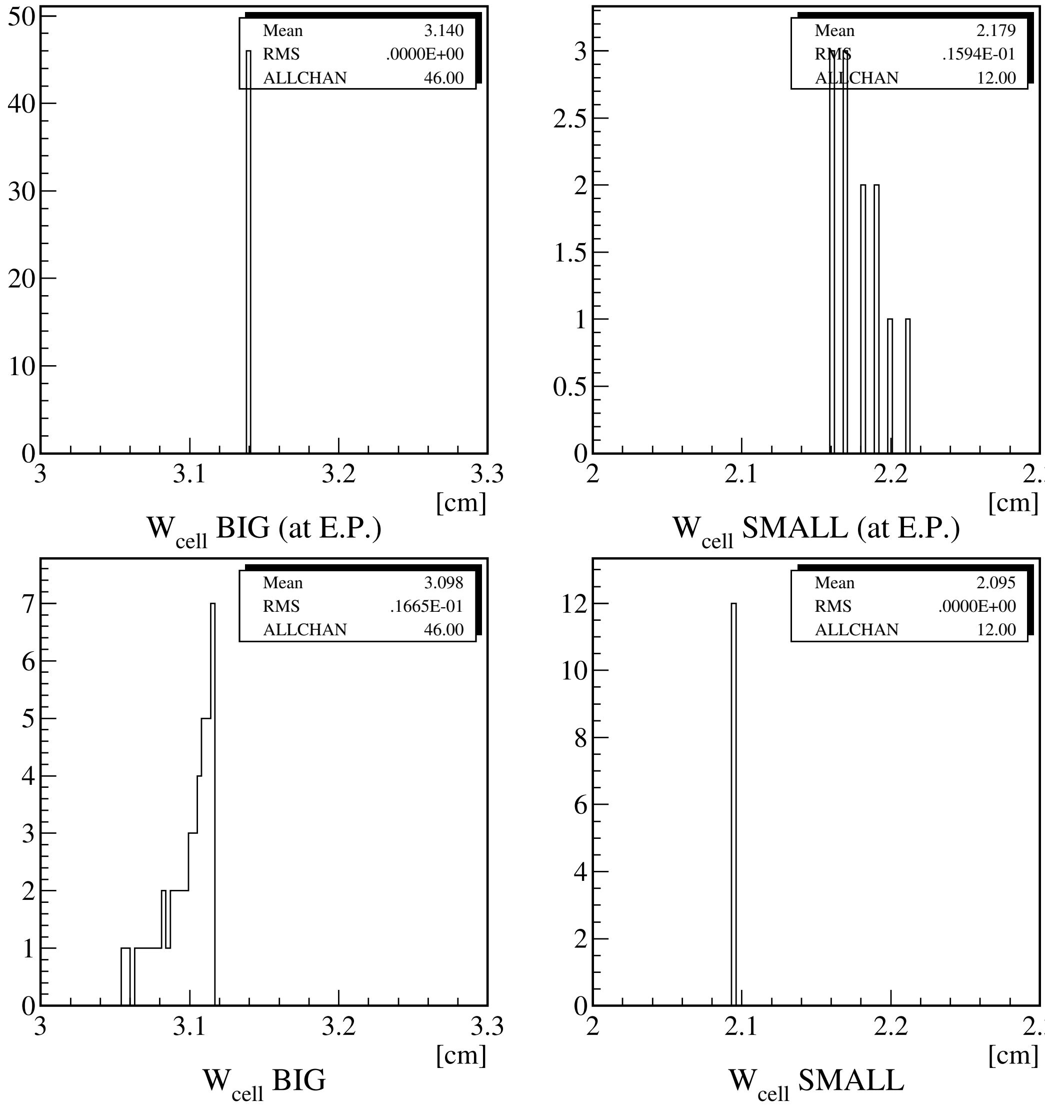

Fig. 13: *Cell width distributions. The cases of small and big cells,* $z = 0$, $z_{\mathrm{E.P.}}$, *are presented.*

REFERENCES

1. The KLOE Collaboration, *The KLOE Central Central Drift Chamber, Addendum to the Technical Proposal*, LNF-028/1994 (1994).
2. A. Andriakov *et al.*, *KLOE Metric (reference systems, numbering/naming conventions, units)*, KLOE note n. 115 (Sep. 1994).